



# Project 067 Impact of Fuel Heating on Combustion and Emissions

## Purdue University

### Project Lead Investigator

Robert P. Lucht  
Ralph and Bettye Bailey Distinguished Professor of Combustion  
School of Mechanical Engineering  
Purdue University  
West Lafayette, IN 47907-2088  
765-714-6020  
Lucht@purdue.edu

## University Participants

### Purdue University

- P.I.s: Dr. Robert P. Lucht and Dr. Carson D. Slabaugh
- FAA Award Number: 13-C-AJFE-PU-038
- Period of Performance: October 1, 2020 to September 30, 2021
- Task:
  1. Investigate the effects of fuel heating on combustion and emissions for aviation gas turbines

## Project Funding Level

Project 67 is funded by the FAA at the level of \$250,000 for the project period June 5, 2020 to June 4, 2021, and an additional \$250,000 for the time period from June 5, 2021 to September 30, 2022. The required cost sharing 1:1 match of \$500,000 is provided by Purdue University.

## Investigation Team

- PI for the project is Professor Robert P. Lucht. Professor Lucht is the major advisor for Colin McDonald.
- Co-PI is Professor Carson D. Slabaugh. Professor Slabaugh is the major advisor for John Philo and Tristan Shahin.
- PhD graduate students are Colin McDonald, John Philo and Tristan Shahin. The graduate students are responsible for the design of system components, such as the fuel heating system, and will be responsible for executing test operations. Research Engineer Dr. Rohan Gejji is also working on the project, is helping the graduate students with their design projects, and will be supervising the test operations.

## Project Overview

The goal of this project is to evaluate the effects of heating jet fuel before injection in an aviation gas turbine combustor on the combustion efficiency, pollutant emissions, and dynamics. In an aircraft engine, heat that would otherwise be wasted can be directed into the fuel to increase its sensible enthalpy before injection. Thermochemistry dictates that this increase in sensible enthalpy must lead to lower fuel consumption for a given combustor exit temperature. However, the effects of elevated fuel temperature on combustion performance characteristics (such as the fuel spray pattern, spatial distribution of reaction zones, pollutant emissions, and combustion dynamics) are not yet well understood. We will perform experiments with heated fuels by using a piloted, partially premixed fuel injector located in an optically accessible combustor. This process will allow us to apply advanced laser diagnostic techniques to compare the behavior of the combustor at different fuel temperatures over a wide range of operating conditions.

The platform for the planned experiments is the Combustion Rig for Advanced Diagnostics (COMRAD). The test rig, shown in Figure 1, is designed to operate at steady-state conditions with thermal powers as high as 8 MW, inlet air pressures ( $P_3$ )



as high as 4.0 MPa, and inlet air temperatures ( $T_3$ ) as high as 1000 K. To facilitate operation at these conditions, the test article is made out of aviation-grade alloys and thoroughly water-cooled, and the inner windows are film-cooled with heated nitrogen. Before this project, extensive testing with ambient-temperature fuels was performed in this rig, with a focus on 5- and 10-kHz particle image velocimetry (PIV) measurements in the downstream boundary condition window section, and 50- and 100-kHz PIV measurements in the flame zone.

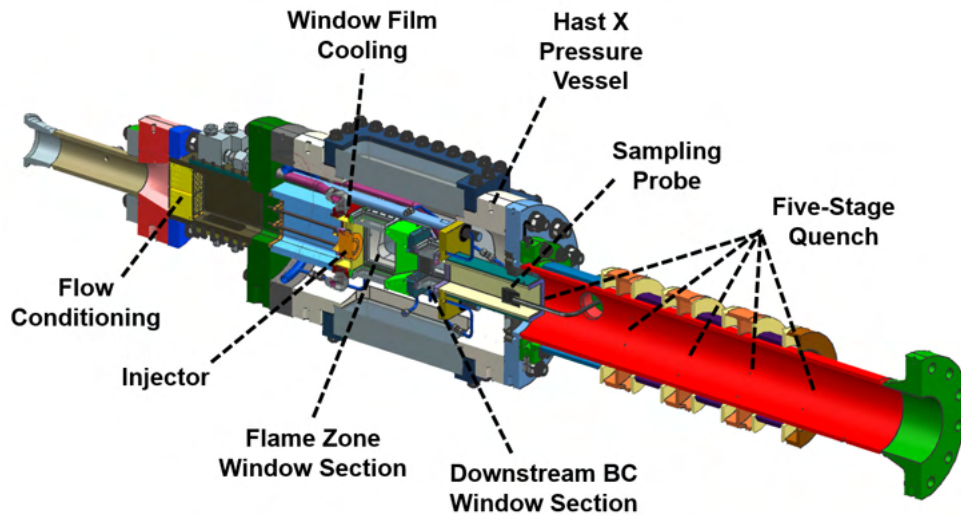


Figure 1. Schematic diagram of the Combustion Rig for Advanced Diagnostics (COMRAD).

## Task 1 - Investigate the Effects of Fuel Heating on Combustion and Emissions for Aviation Gas Turbines

Purdue University

### Objective

The goal of this project is to determine the effects of fuel heating on the performance of aviation gas turbines. Fuel heating can potentially lead to higher efficiency, but can also lead to changes in the fuel distribution pattern and in the location of reaction zones in the combustor. These changes may also impact pollutant emissions and combustion dynamics during engine operation. We will perform experiments using heated fuels and will measure the fuel distributions, reaction zone distributions, pollutant emissions, and combustion dynamics at a range of fuel temperatures from near room temperature to above the supercritical temperatures for hydrocarbon fuels.

### Research Approach

We will perform experiments with heated fuels by using a piloted, partially premixed fuel injector located in an optically accessible combustor. This setup will allow us to apply advanced laser diagnostic techniques to compare the behavior of the combustor at different fuel temperatures over a wide range of operating conditions. These advanced diagnostic techniques include fuel planar laser-induced fluorescence (PLIF) imaging to monitor fuel distribution patterns, hydroxyl ( $OH$ ) radical PLIF ( $OH$  PLIF) imaging to monitor reaction zones, and PIV to measure the flow-fields. We will also measure emissions with probe sampling and will use pressure transducers to measure combustion dynamics.

### Milestones

The milestones for the work performed in fiscal year 2021 are listed below:

1. A fuel heater capable of heating three independent circuits of jet fuel to 700 K at 4.0 MPa was developed and successfully deployed in the test cell.
2. The operational sensitivity of the experiment to fuel temperature on the emissions and flame structure was evaluated for a range of operating conditions through emissions sampling with a Fourier-transform infrared



spectroscopy (FTIR) gas analyzer and 50-kHz  $OH^*$  chemiluminescence imaging. Measurements were performed at 1.0-MPa and 2.0-MPa inlet air pressures at a range of equivalence ratios and fuel temperatures.

3. Detailed measurements of the flow-field in the combustion zone were conducted through the application of 10-kHz stereoscopic PIV (SPIV) measurements at a down-selected range of operating conditions from the parametric survey with emissions measurements.
4.  $OH$  PLIF measurements were successfully demonstrated at 10 Hz to characterize the reaction zone location as a function of fuel temperature.

## Major Accomplishments

In the current reporting period, we successfully characterized the effects of injection of heated jet fuel on the combustion efficiency and emissions in a model aviation gas turbine combustor. Toward this goal, we designed and demonstrated the operation of a fuel heating system capable of heating three independent fuel circuits to temperatures and pressures exceeding the critical point of the fuel. Combustion experiments with heated fuel were performed at a range of equivalence ratios at pressures of 1.0 and 2.0 MPa. The initial tests focused on emission sampling and high-speed flame imaging to characterize the effects of fuel heating on the combustion process. After a survey of emissions was completed, down-selected cases were characterized in detail with SPIV and  $OH$  PLIF measurements.

### A. Fuel Heater Development

The fuel heater is designed to heat a continuous flow of 50 g/s of jet fuel up to 700 K at pressures up to 4 MPa. For heating, the fuel flows through stainless steel tubing that is wrapped between pairs of copper blocks heated with cartridge heaters. In total, five pairs of copper blocks and 100 cartridge heaters are used, resulting in a combined heating power of 81 kW. The cartridge heaters are split into 20 independently controlled zones of five cartridges, enabling flexibility and control of the fuel temperature of both the pilot and main fuel circuits exiting the heater. An image of the assembled fuel heater is shown in Figure 2.



**Figure 2.** Photograph of the assembled fuel heating system.

The fuel in three independent circuits is carried from the heater to the experiment in stainless steel tubing that is trace heated and insulated to minimize heat loss. The fuel flow to the heater and the experiment is controlled with metering valves and measured with Coriolis flow meters. The temperature of the fuel is monitored in the fuel heater (to ensure that no phase change is encountered) and immediately upstream of the injector. An inert gas purge circuit is used to avoid collection of

stagnant fuel in the heater and the tubing to the experiment when fuel is not flowing to the experiment. This purge displaces the fuel to a collection tank through a bypass circuit and counter-flow heat exchanger that cools the fuel temperature to ambient temperature with water as the heat transfer medium. The plumbing and instrumentation diagram shown in Figure 3 details the fuel supply layout.

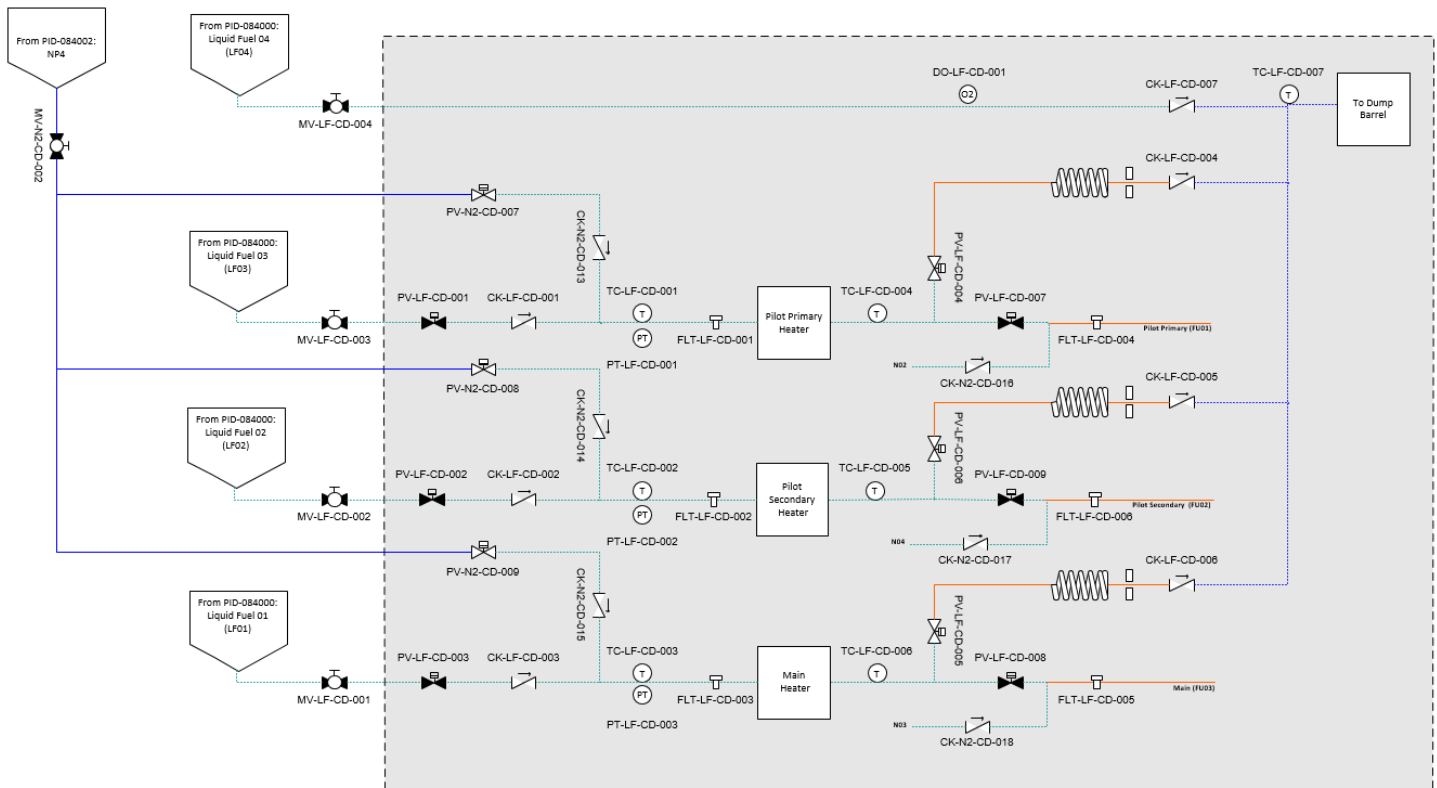
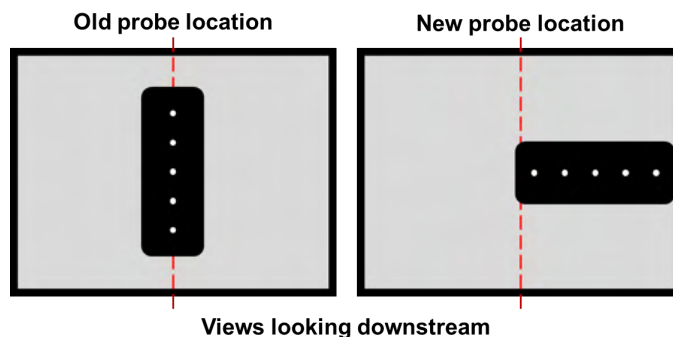


Figure 3. Plumbing and instrumentation diagram for the heated fuel supply to the experiment.

Fuel heater operation was successfully demonstrated after completion of the assembly process, first by heating fuel independently of the combustor and finally in combustion experiments. Sufficient control to enable repeated measurements in the combustor with fuel temperatures of 370 K, 470 K, and 570 K was demonstrated for a range of fuel flow rates to enable understanding of trends in combustion efficiency in the experiment.

**B. Emissions Sampling and OH\* Imaging**

Emissions sampling began with unheated, ambient-temperature fuel to test the emissions sampling system. For these measurements, a sampling probe was placed in the center of the exhaust channel as shown in the “old” configuration in Figure 4. The initial results did not yield the expected trends because the measurement was missing the near-wall region. Other experiments have shown that gradients in product gas species concentrations exist in the radial direction in similar burner configurations; therefore, the near-wall region was expected to have a different gas composition from that of the bulk flow in the combustor. For the measurements with heated fuel, the probe was reconfigured and placed offset to one side of the exhaust channel, as shown in the “new” configuration in Figure 4. This updated sampling configuration provided a more representative sample of the exhaust. While the emissions samples were being acquired, OH\* chemiluminescence images were acquired at 50 kHz. A high-speed camera (Phantom v2512) was coupled to an ultraviolet (UV)-sensitive intensifier (Lambert HiCATT) to image flame emission optically filtered to 320 ± 20 nm. These images captured a line-of-sight integrated representation of the heat release in the experiment.



**Figure 4.** Emissions probe installation locations. The new probe location was used for all measurements reported herein.

Experiments with heated fuel began in March of 2021 after the fuel heater fabrication was completed. The emissions sampling and  $OH^*$  chemiluminescence imaging were performed at the conditions listed in Table 1. A range of fuel-air equivalence ratios were tested for three fuel temperatures at an inlet air pressure of 1.0 MPa. Additional measurements were taken at an inlet air pressure of 2.0 MPa at the highest fuel temperature to determine the effect of increased pressure on emissions. Because the fuel heater heats the pilot and main fuel circuits independently, the fuel temperature reported herein is a mass-flow-weighted average of the fuel temperature of each circuit. The inlet air temperature and the pressure drop across the injector were held constant for all conditions. Measured quantities of key species are shown in Figures 6–9. Combustion efficiency is defined according to Eq. 1, in which the emissions index ( $EI$ ) is the quantity of a species in grams of the species per kilogram of fuel consumed, and  $H_c$  is the heating value of the fuel.

**Table 1.** Test conditions. The equivalence ratio was varied within the specified range for each set of conditions.

$P_3$ (MPa)	$T_3$ (K)	Overall $\phi$	$T_{fuel,av}$ (K)	Pilot/Total (%)	$\dot{m}_{air}$ (kg/s)
1.00 ± 0.12	755 ± 17	0.37 - 0.50	373 ± 6	30.0 ± 1.0	0.585 ± 0.005
		0.37 - 0.47	473 ± 7		
		0.36 - 0.51	568 ± 3		
2.00 ± 0.06		0.33 - 0.47	584 ± 2		1.170 ± 0.012

$$\eta_b = \left[ 1.00 - 10.109 \frac{EI_{CO}}{H_c} - \frac{EI_{UHC}}{1000} \right] \quad (1)$$

From the emissions results, several observations were made regarding pollutant formation in the combustor. As shown in Figure 5(a), the combustion efficiency increased with an increase in fuel temperature, particularly at the lower equivalence ratios studied herein. Combustion efficiency was also higher at increased inlet air pressures, as shown in Figure 5(b). Concomitant decreases in CO and unburnt hydrocarbons (UHC) with increasing fuel temperatures and pressures are shown in Figures 6 and 7, respectively. Another important result from the emissions testing is shown in Figure 8: nitrogen oxide ( $NO_x$ ) production increased by 20%–30% with an increase in  $T_{fuel,av}$  from 373 K to 473 K, and an additional increase of 10%–15% was observed for lower equivalence ratios when  $T_{fuel,av}$  was increased again to 568 K. At equivalence ratios of approximately 0.43 and above, no conclusive change in  $NO_x$  was observed between  $T_{fuel,av} = 473$  K and  $T_{fuel,av} = 568$  K. The results in Figure 9 show that, for an increase in pressure at constant fuel temperature, the measured  $NO_x$  emissions index indicates a pressure dependence with an exponent between approximately 0.4 and 0.8. For all fuel temperatures at an inlet air pressure of 1.0 MPa, the ratio of NO to  $NO_x$  was nearly constant between fuel temperatures but varied strongly with the

equivalence ratio. Likewise, this ratio did not vary substantially with the increase in pressure but again varied strongly with the equivalence ratio. Detailed laser-based diagnostics are in progress to study the flow and flame features that led to these measured changes in pollutant emissions.

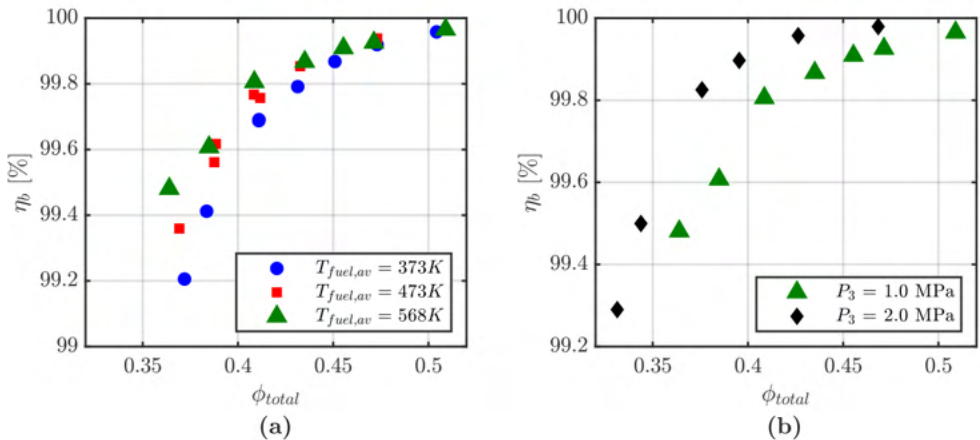


**Figure 5.** Combustion efficiency, measured at a range of equivalence ratios at (a) three different fuel temperatures with  $P_3 = 1.0$  MPa and (b) two different inlet air pressures with  $T_{fuel,av} = 573$  K.

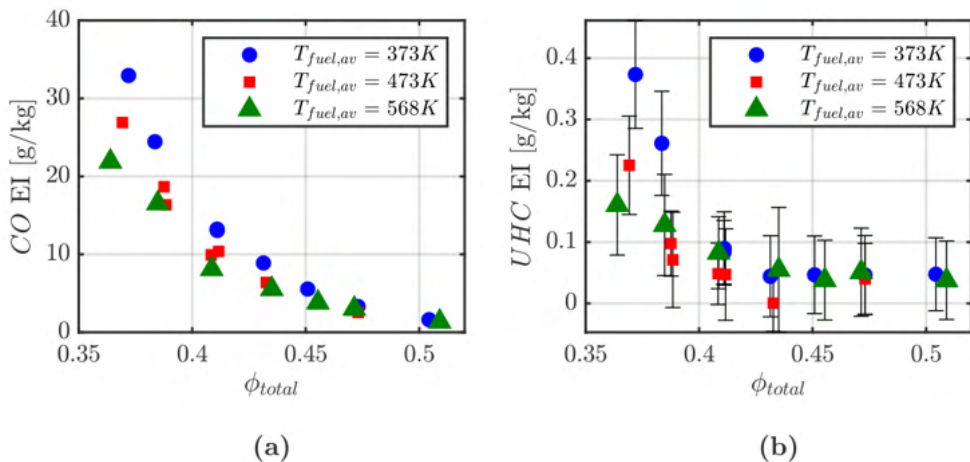


**Figure 6.** Carbon monoxide and unburnt hydrocarbon emissions, measured at a constant inlet air pressure of 1.0 MPa.

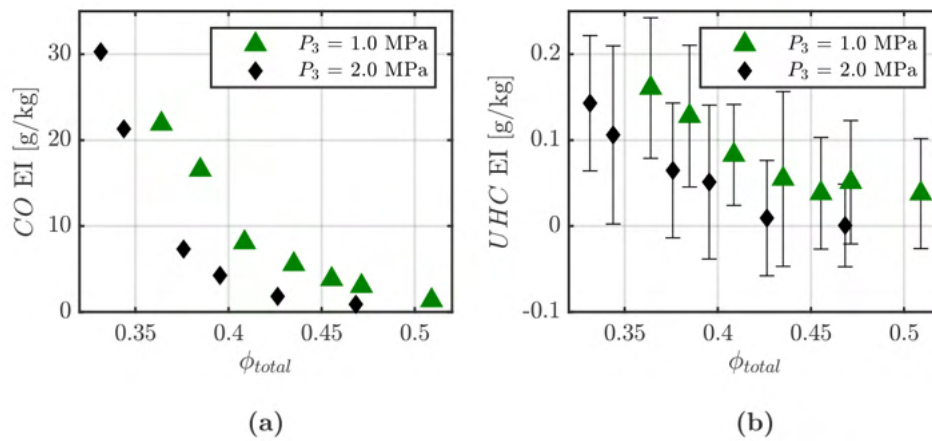


Figure 7. Carbon monoxide and unburnt hydrocarbon emissions, measured at a constant  $T_{fuel,av}$  of 573 K.

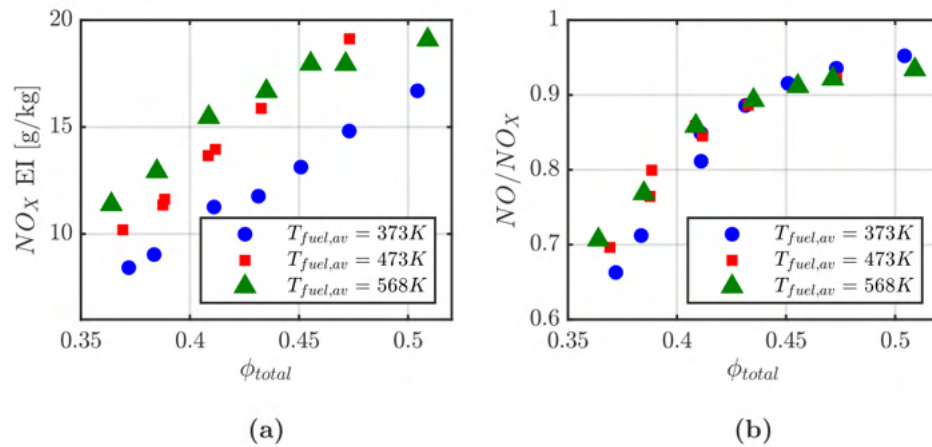


Figure 8.  $NO_x$  emissions, measured at a constant inlet air pressure of 1.0 MPa.

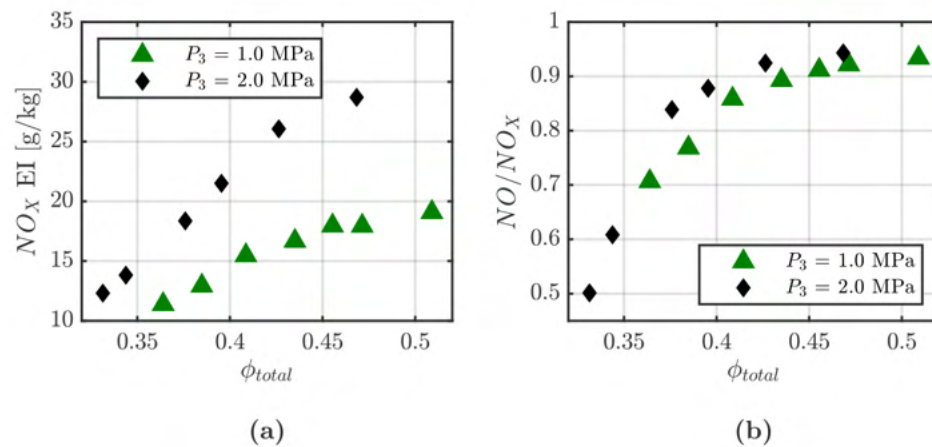
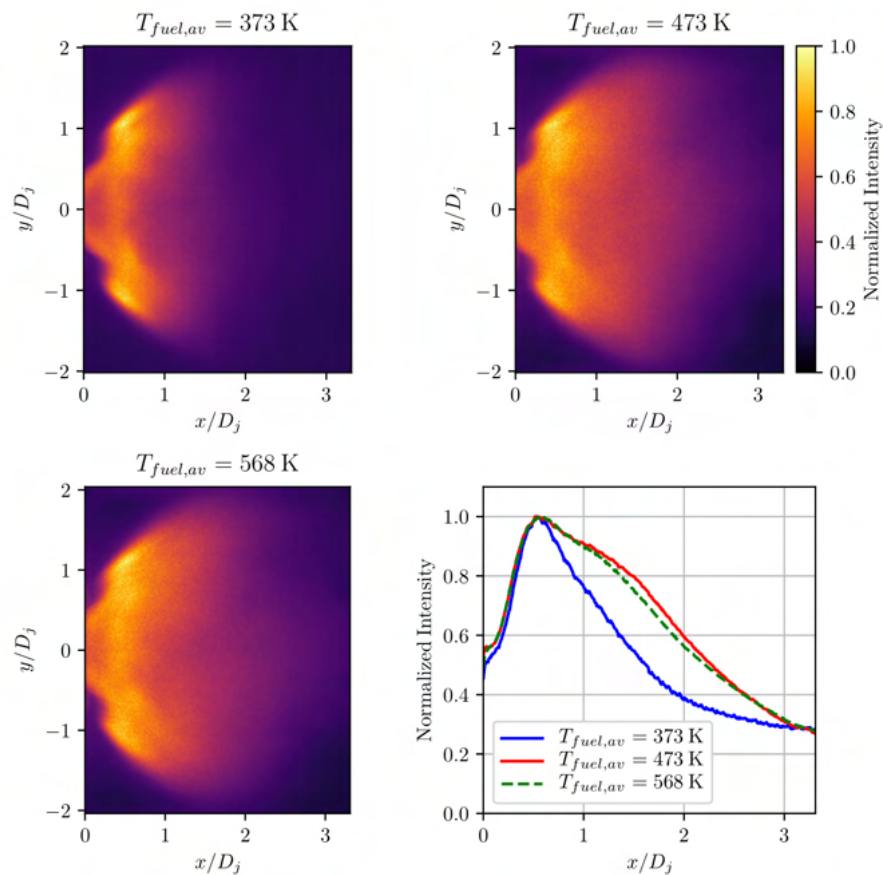


Figure 9.  $NO_x$  emissions, measured at a constant  $T_{fuel,av}$  of 573 K.



The  $OH^*$  chemiluminescence images showed significant changes in the spatial distribution of flame luminosity when the fuel temperature and inlet air pressure were varied. Figures 10 and 11 illustrate the observed changes. When the fuel temperature was increased at a constant inlet air pressure of 1.0 MPa, the time-averaged flame grew appreciably longer, especially for the increase in  $T_{fuel,av}$  from 373 K to 473 K. This finding is further clarified by the line plot in Figure 10, which shows the vertically summed intensity along each average flame. Analogous images showing the increase in pressure with constant fuel temperature of 573 K are presented in Figure 11, which show that the increased pressure led to a subtle increase in the presence of  $OH^*$  in the downstream portion of the flame. Using the region denoted by the white rectangle in Figure 11, the intensity was summed in the vertical direction to show how the flame changes in the region where the main reactants interact with the pilot flame. The results shown in Figure 12 indicate a small shift in the main flame toward the face of the injector in the region near  $x/D_j = 0.3$  for cases with  $P_3 = 1.0$  MPa as well as the lengthening effect seen in other figures. For the increase in inlet air pressure, no discernible change was observed in the near-injector portion of the flame in the selected area.



**Figure 10.** Variation in average flame luminosity with changes in  $T_{fuel,av}$ . The plot at the lower right shows the luminosity summed in the  $y$  direction as a function of  $x/D_j$ .

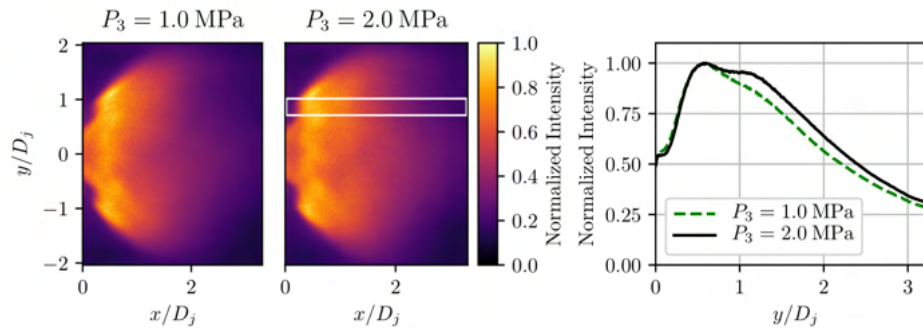


**Figure 11.** Variation in average flame luminosity with changes in  $P_3$ . The plot in the lower right shows the luminosity summed in the  $y$  direction as a function of  $x/D_j$ . The white rectangle on the right flame image corresponds to the area used for the plot in Figure 12.

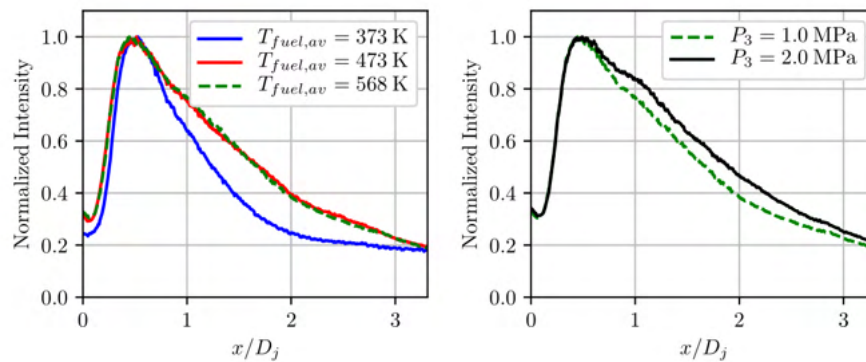


**Figure 12.** Variation in horizontally summed average flame luminosity in the region between  $y/D_j = 0.7$  and  $y/D_j = 1.0$ , indicated with a white rectangle in Figure 11.

### C. Stereoscopic PIV Measurements

After completing the parametric survey of operating conditions with emissions sampling in May of 2021, we transitioned to applying laser diagnostics to better understand how the flow and flame change relative to the observed emissions trends. We began with 10-kHz stereoscopic PIV (SPIV) with simultaneous 10-kHz  $OH^*$  chemiluminescence. SPIV enables all three components of velocity to be measured in a plane coincident with the vertical centerline of the combustor. The diagnostic configuration for this measurement is depicted in Figure 13. A dual-cavity, diode-pumped solid-state (DPSS) Nd:YAG-based laser provides pulse doublets of 532-nm light at 10 kHz with a pulse separation of 3.0  $\mu$ s. The laser pulse separation was selected to optimize the particle displacement between slow-moving regions in the recirculation zones and high velocities in the reactant jets. Four cylindrical lenses form and collimate the laser sheet, which is then directed along the centerline of the combustor using a series of mirrors. The beam is focused such that the beam waist is located just below the measurement domain, and the resulting sheet thickness is less than 1 mm. The air is seeded with 200-nm zirconia ( $ZrO_2$ ) particles with an independently controlled and metered air circuit. Two high-speed CMOS cameras (Phantom V2512) are used to capture the scattered light signal with a spatial resolution of 63  $\mu$ m/pixel for the measurement field of view. The cameras are located on opposite sides of the rig, angled approximately 30° relative to the laser sheet. A 200-mm focal-length,  $f/4.0$  lens is mounted to each camera with a Schempflug adapter, which ensures that the entire measurement domain is in focus. An ultra-steep bandpass filter centered at 532 nm with 3-nm full width at half maximum is used to isolate the signal from background flame luminosity, and an additional wide-band bandpass filter is used to block the remaining wavelengths of light within the CMOS sensor sensitivity range. The camera setup for the  $OH^*$  chemiluminescence measurement is the same as that for the above emissions results, but with a different CMOS camera that limits the repetition rate to 10 kHz for the given image resolution.

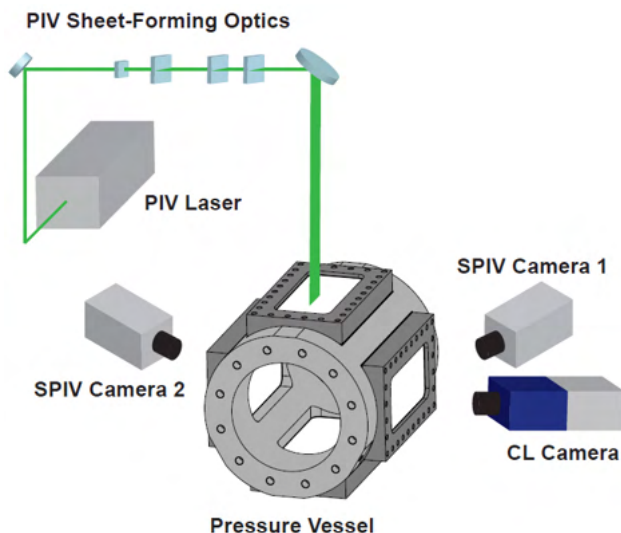


**Figure 13.** Schematic diagram of the stereo PIV measurement system.

Multiple difficulties arise in performing PIV measurements in high-pressure reacting flow-fields, especially those using liquid fuels. Mie scattering off unevaporated fuel droplets can saturate local regions of the acquired images, thus hiding any seed particles that are present. Large density gradients in the flow-field can lead to difficulties in supplying a uniform seed density throughout the measurement domain, and the wide range of velocities present requires a measurement with high dynamic range. Glare from the scattered laser light off surfaces in the combustor can also reduce the signal-to-noise ratio, particularly as seed particles are deposited on the combustor windows. In the present experiment, PIV data were acquired during 5- to 10-second seed flows, which could occur approximately 10 times on a given test day before window fouling from seed particles began to affect the measurement quality. For all fuel temperatures tested, most of the liquid fuel was evaporated before entering the measurement domain, and primarily small droplets remained that could not be distinguished from the seed particles.

Many of the above issues can be addressed either in the experimental configuration or during data processing. The SPIV image processing and vector calculation were performed using LaVision DaVis 8.4. Background intensity was removed by subtraction of the minimum intensity using a seven-image sliding window, then subtracting a sliding average over a window of  $9 \times 9$  pixels. Intensities were then normalized using the minimum and maximum intensity in a window of  $7 \times 7$  pixels. Before performing the vector calculation, all images were spatially calibrated with the DaVis self-calibration feature. The vector calculation was performed using multiple passes with decreasing interrogation window size, with a final interrogation window of  $32 \times 32$  pixels and 75% overlap. Spurious vectors were removed after the vector calculation using a universal outlier detection median filter. The resulting vector fields yielded a high percentage of valid vectors, as shown in Figure 14. For most locations in the measurement domain, a valid vector was present for more than 90% of the time series. Issues with glare on the burner face and the large out-of-plane velocity component in the main reactant flow in the top-left and bottom-left corners reduce the vector yield in those locations.

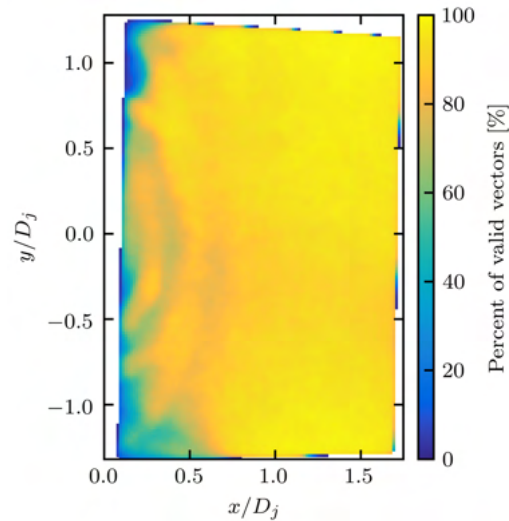


**Figure 14.** Percentage of valid vectors at each location in the measurement domain for a typical test.

Multiple techniques exist to fill in missing data in PIV measurements. One option involves spatial interpolation of an instantaneous vector field to replace gaps in the data based on the velocity at surrounding points. This procedure can be performed simply by iteratively taking the average of surrounding points with empty spaces until all gaps are removed. More advanced spatial interpolation techniques, such as Kriging interpolation, can yield better results but have the drawback of increased computational cost. For this work, we used gappy proper orthogonal decomposition (GPOD) to fill in the gaps in the data with both spatial and temporal information from the measured vector fields. This method performed POD iteratively, using an increasing number of modes to reconstruct the velocity fields, until the error calculated based on artificial gaps in the data reached a minimum. A median filter was applied to the reconstruction at the end of each iteration to determine whether to use the newly predicted value of velocity as the initial guess for the next iteration. This technique has been shown to yield reconstruction errors as good as or better than those with Kriging interpolation, with a much lower computational cost. For each condition tested, 2,000 vector fields were generated using DaVis and filled with GPOD. GPOD was performed on each component of velocity independently, and each component generally required between 800 and 1,000 modes to reconstruct the velocity field before the minimum error was achieved. The results from this process are illustrated in Figure 15 with a sample velocity field. The original axial velocity field with gaps in the data is shown in Figure 15(a), and a smaller region of the velocity field is highlighted in Figure 15(b). Figure 15(c) shows the resulting velocity field after the missing data were filled with GPOD, thus yielding reasonable results for the missing velocity at all points.

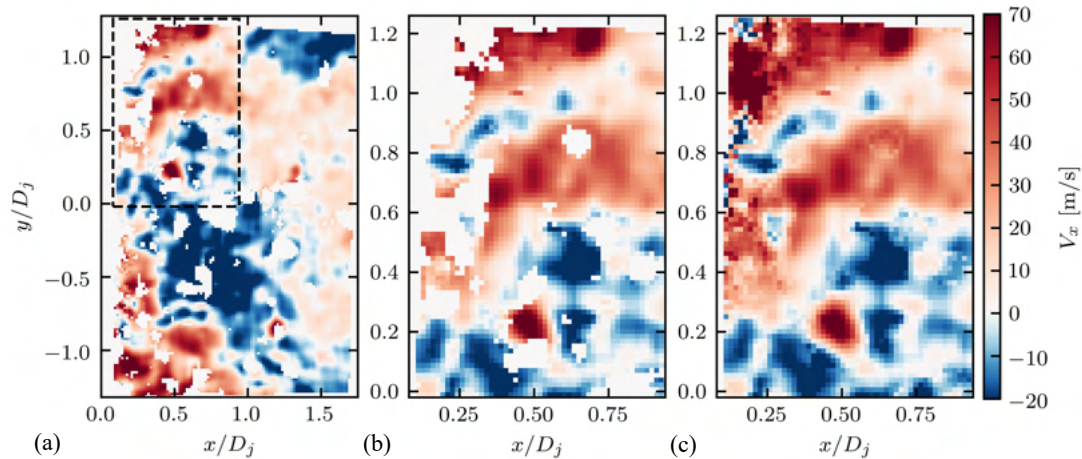


**Figure 15.** (a) Sample original axial velocity field. (b) Original axial velocity field in the region denoted by the dashed box in (a). (c) Original velocity field from (b), with missing data filled in with MF-GPOD.

To date, high-quality SPIV data have been recorded at 12 conditions at an inlet air pressure of 1.0 MPa and at four conditions at an inlet air pressure of 2.0 MPa. A total of 2,000 vector fields have been calculated at each condition, and the missing vectors have been filled in with GPOD. Detailed analysis of this data is ongoing and should be completed early in the upcoming year of the project. Figures 16–18 display some initial results from this work. The average magnitude of the velocity over 2,000 vector fields is depicted in Figure 16, with the important flow features labeled. Annotation 1 is the high-velocity region corresponding to the main reactant flow, and annotation 2 is the high-velocity region corresponding to the pilot reactant flow. Because these features are axisymmetric, they are also present in the bottom half of the mean velocity field. Annotation 3 corresponds to the inner recirculation zone (IRZ) that forms downstream of a bluff-body feature on the injector, between the two high-velocity regions. Annotation 4 is the central recirculation zone (CRZ), a low-velocity region that provides high-temperature product gases to the flame root, thereby sustaining stable combustion. Unlike the pilot and main reactant jets, this recirculation zone is not symmetric across the horizontal centerline, probably because of the rectangular shape of the combustor cross-section.

To compare the mean velocity fields over the range of conditions tested, iso-contours defining the border between different features in the flow-field were determined. The mean axial velocity field is shown in Figure 17(a) for the same case shown in Figure 16. The black lines correspond to iso-contours where the axial velocity is equal to 5 m/s, as determined using a marching squares algorithm. The iso-contours were set to 5 m/s, because this value allowed the lines to follow the shear layer between the pilot reactant jet and CRZ for both the top and bottom halves of the flow-field, and biased the lines toward regions of higher shear. An iso-contour also surrounds the region of positive axial velocity along the centerline of the combustor that occurs inside the CRZ. These iso-contours of  $V_x = 5$  m/s were determined in a similar manner for the mean flow-fields for all conditions tested. Figure 17(b) shows three iso-contours on the same plot corresponding to conditions at three different fuel temperatures with approximately the same equivalence ratio and inlet air pressure. At the upstream portion of the flow-field, near the injector, no clear difference is present between the iso-contour locations, but the lines begin to diverge further downstream. The circled region highlights the area where the differences are most evident over all conditions tested. This region coincides with the interaction between the pilot and main reactant jets. As the fuel temperature rises, the iso-contours move downstream.

The iso-contours generated from all 16 cases of PIV data are compared in Figure 18. A single value that defines the location of each iso-contour was determined by taking the average axial location of the part of the iso-contours within the circled region in Figure 17(b). The minimum value of the average iso-contour axial location in each plot in Figure 18 was subtracted from each point to give the relative positions of the iso-contours. As shown in Figure 18(a) the iso-contours move downstream both as the fuel temperature rises and as the equivalence ratio is increased. Additionally, similar to the changes in measured  $\text{NO}_x$  during the emissions sampling, the change in position from  $T_{fuel,av}$  of 367 K to 486 K is greater than the change from 486 K to 577 K. This downstream shift in the location of the iso-contours may correspond to the increased  $\text{OH}^*$  chemiluminescence intensity present in the downstream region as the fuel temperature is increased, and the planned  $\text{OH}$  PLIF measurements will help clarify the observed changes. As the inlet air pressure is increased from 1.0 MPa to 2.0 MPa, no

clear shift occurs in the iso-contour location for a given equivalence ratio and fuel temperature, as shown in Figure 18(b). This result is expected, because the injector pressure drop is maintained as the pressure rises.

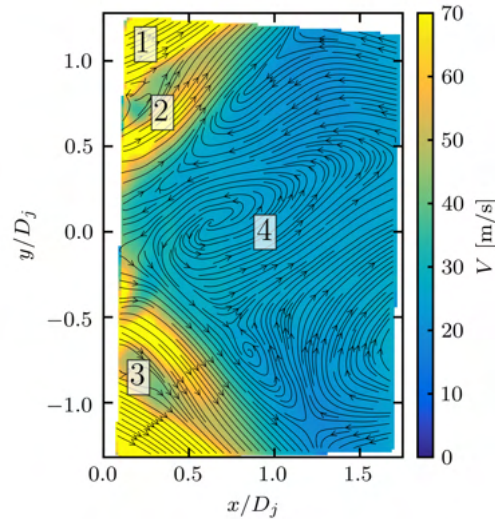


**Figure 16.** Mean velocity field with streamlines overlaid for  $P_3 = 1.0$  MPa,  $T_{fuel,av} = 367$  K, and  $\phi = 0.36$ .

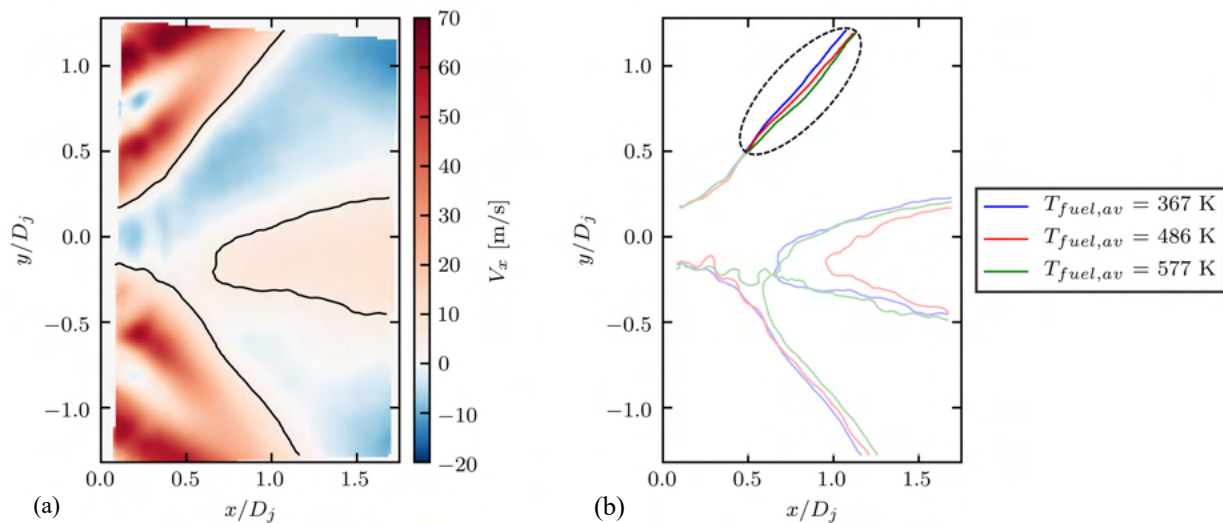


**Figure 17.** (a) Mean axial velocity field for  $P_3 = 1.0$  MPa,  $T_{fuel,av} = 367$  K, and  $\phi = 0.36$  with iso-contours of mean  $V_x = 5$  m/s denoted by black lines. (b) Iso-contours of mean of  $V_x = 5$  m/s for three fuel temperature conditions with  $P_3 = 1.0$  MPa and  $\phi = 0.36$ . The circle highlights the region where the largest changes between conditions occur.

Further analysis of the acquired PIV data is ongoing, and includes extending the analysis using iso-contours to instantaneous flow-fields in addition to the mean flow-fields. The time series of iso-contours can be used to condition various turbulent flow parameters, such as shear and vorticity. Averaging the data only at locations and times when an iso-contour is present can help elucidate some of the differences between the average flow-fields.

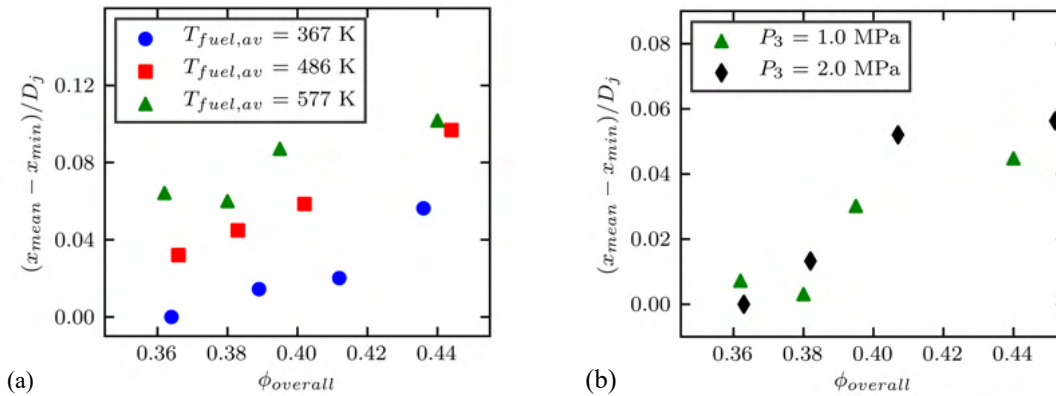


**Figure 18.** Mean axial location of the portion of the stagnation line in the circled region in Figure 17(b) for all conditions tested. Values are plotted relative to the minimum value of the mean axial stagnation line location for (a) constant inlet air pressure of 1.0 MPa and (b) constant  $T_{fuel,av} = 577\text{ K}$ .

#### D. OH PLIF Imaging

OH PLIF imaging was successfully demonstrated in August 2021 at 10 Hz, allowing a region approximately 40 mm in width to be captured in each frame. For this experiment, a 532-nm pump laser beam was directed into a dye laser filled with rhodamine 590 dye. The output of the dye laser was tuned to an electronic transition in the Q branch of the OH molecule near 283 nm, thus resulting in the short-lived fluorescence (for several nanoseconds) of a fraction of these molecules as they relaxed back to their ground electronic state. With each laser shot, this fluorescence was captured by a CMOS camera (Phantom v2512) with an s-sensitive intensifier (Lambert HiCATT). Locations with high gradients in OH (particularly in the upstream part of an image), are indicative of the reaction front (or “flame surface”), where the highest levels of heat release occur.

Because of variations in intensity along the laser sheet and absorption effects, OH PLIF images cannot be treated as quantitative maps of OH concentration. Instead, these images must be processed to generate useful statistics. By converting the images into binarized maps showing which regions contain OH, quantitative information about the flame can be obtained. To do so, a robust edge detection method is required. For this project, a method known as semantic segmentation is used to separate each OH PLIF image into regions of signal and background. Semantic segmentation involves training a convolutional neural network to recognize these regions by learning from human-labeled images. To date, 176 images have been manually labeled, of which 156 were used as training images, and 20 were used as validation images. From this dataset, the semantic segmentation model has exceeded, in accuracy, most of the thresholding methods typically used by our group and others. Two representative images and their detected edges are shown in Figure 19. Further refinement of the edge detection model is in progress, and the model will be applied to future OH PLIF images taken for this project. At present, too few OH PLIF experiments have been performed to draw meaningful conclusions regarding differences in the flame between conditions, but sufficient results are expected early in the next year of the project.

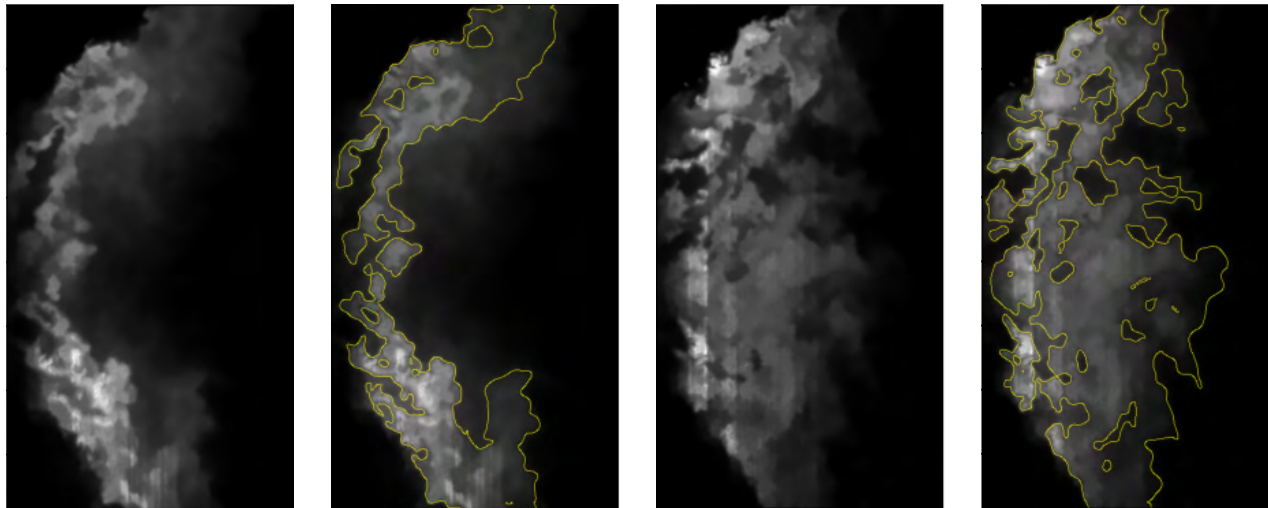


Figure 19. Two representative *OH* PLIF images with detected edges from the semantic segmentation model shown in yellow on duplicate images.

## Publications

### Published conference proceedings

McDonald, C. T., Philo, J. J., Shahin, T. T., Gejji, R. M., Slabaugh, C. D., & Lucht, R. P. (2021). Effect of fuel temperature on emissions and structure of a swirl-stabilized flame [Presentation]. AIAA Propulsion and Energy 2021 Forum, Virtual Meeting. Paper Number AIAA 2021-3480.

## Outreach Efforts

None

## Awards

None

## Student Involvement

Three PhD graduate students are working on the project. The project provides outstanding research experiences for the graduate students, including the design of system components for, and the operation of, a sophisticated aviation gas turbine combustion test rig, as well as application of advanced laser diagnostic methods for measurements in this test rig. As noted above, the graduate students have been responsible for the design of system components, such as the fuel heating system, and for executing test operations.

## Plans for Next Period

During the next year of the project, we plan to perform more experiments with heated fuel with various diagnostic techniques. Multi-scale PIV, *OH* PLIF, fuel PLIF, and coherent anti-Stokes Raman scattering (CARS) measurements will be performed to further characterize the flow-fields at the range of operating conditions considered for the emissions measurements.

### **A. Multi-scale PIV Measurements**

We will perform multi-scale PIV to simultaneously measure the in-plane components of velocity over the majority of the flame at 10 kHz and in a more localized area at 100 kHz. Figure 20 shows the expected field of view (FOV) for each of these measurement regions. The 10 kHz 2D2C PIV will have the same spatial resolution as the previous 10-kHz stereo PIV measurements, but the 100-kHz 2D2C PIV will be configured to have a spatial resolution with twice as many pixels per millimeter. The improved spatial and temporal resolution of the 100-kHz PIV will enable measurements of small-scale flow dynamics, such as vortex shedding in the shear layer between the pilot and CRZ, that are missed by the 10-kHz PIV. The 10-

kHz measurement will be performed with the same laser as that in the 10-kHz stereo PIV, which provides pulse doublets of 532-nm laser radiation. For the 100-kHz measurements, an Nd:YAG based pulse-burst laser (PBL) along with an optical parametric oscillator (OPO) will be used to provide laser emission tuned to 566 nm for burst durations of 10 ms. Since PIV is an elastic scattering process, the use of two different laser wavelengths is necessary to distinguish the scattering signals from the different laser pulses. Separate high-speed, CMOS cameras with the appropriate optical filters will be used for the two measurements. Extending the standard PIV measurement to this multi-scale configuration will make it possible to resolve how the increase in fuel temperature affects the interactions between flow dynamics over a wide range of scales.

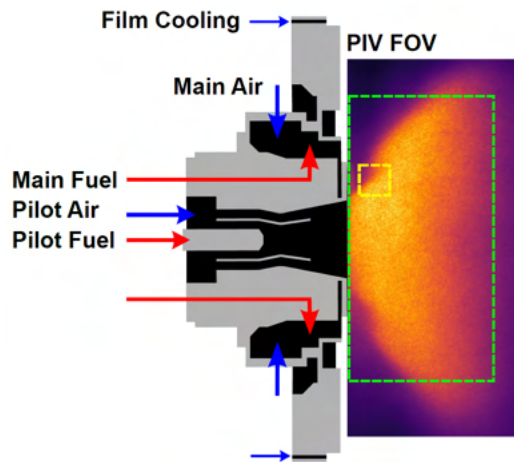


**Figure 20.** Schematic of multi-scale PIV showing expected fields-of-view for the 10-kHz measurement (green box) and the 100-kHz measurement (yellow box) overlaid on a mean  $OH^*$  CL emission field at  $P_3 = 1.0$  MPa and  $\phi = 0.36$ .

**B.  $OH$  PLIF Imaging and Emissions Measurements**

We will continue taking  $OH$  PLIF images while repeating some points from our emissions dataset with a new emissions sampling probe. Because of concerns regarding the potential of unchoked holes to create nonuniform sampling between holes in the current probe, a new emissions probe was designed and is currently being procured. The new design, shown in Figure 21, features a Hastelloy X body with a yttrium-stabilized zirconia thermal barrier coating and internal water cooling passages to ensure survivability. The probe's discrete sample passages enable sampling of species profiles across the exhaust channel, which will not be performed as part of this experiment but may be used for future work.

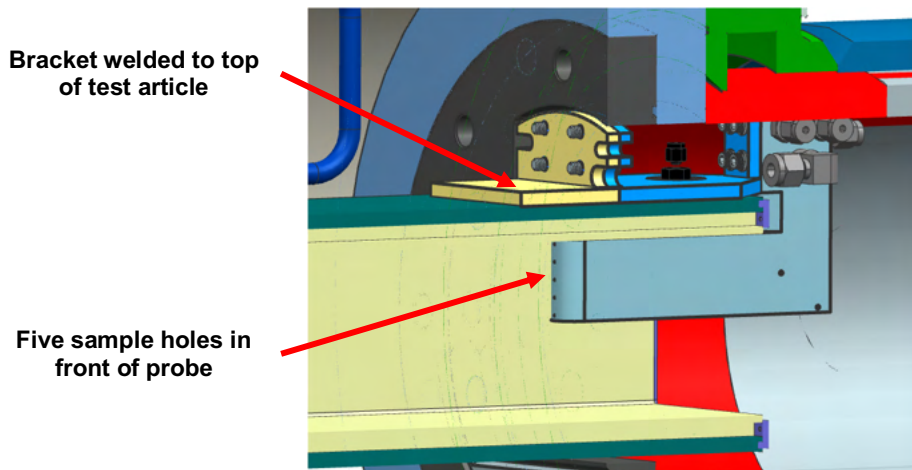


**Figure 21.** CAD rendering of the new emissions probe design.



Additional *OH* PLIF images will be recorded at a down-selected range of equivalence ratios and fuel temperatures similar to those chosen for the stereoscopic PIV measurements, and emissions measurements will be recorded simultaneously. This experiment will create a dataset showing the locations of reaction zones for each condition with the associated changes in emissions. Image analysis will be performed to draw conclusions regarding how the changing reaction zones may affect pollutant production by the flame.

### **C. Fuel PLIF Imaging**

By adding a small percentage of Jet A fuel to our current Fischer-Tropsch fuel, we will raise the aromatic content of the fuel mixture to a level that enables PLIF imaging of the fuel spray from the injector. The 10-Hz pump laser used for *OH* PLIF imaging will also be used for fuel PLIF. By capturing fuel fluorescence in the near-injector region, we will be able to detect changes in the fuel spray pattern that occur with changes in operating conditions, including changes in the fuel temperature. These images will be used in concert with the *OH* PLIF images to provide a more comprehensive understanding of the effects of fuel temperature on the combustion process at the range of equivalence ratios and inlet air pressures considered.

### **D. Coherent Anti-Stokes Raman Scattering (CARS) Measurements**

CARS, a laser-based technique for measuring temperature and species concentration in gases, will be used to measure the temperature in the flame zone of the COMRAD test rig by targeting  $N_2$  molecules. Because fuel heating is expected to change the temperature field within the flame zone, CARS measurements are an important means of characterizing the effect of heated fuel on the flame. The local temperature throughout the flame strongly affects the rates of many combustion reactions, including the formation of nitric oxide. Thus, the CARS measurements will help us understand how fuel heating leads to the measured changes in emissions.